Effect of the interfacial electronic coupling of nickel-iron sulfide nanosheets with layer Ti$_3$C$_2$ MXenes as efficient bifunctional electrocatalysts for anion-exchange membrane water electrolysis

Debabrata Chanda [a,b,*], Karthik Kannan [a,b], Jagadis Gautam [a,b], Mikiyas Mekete Meshesha [a,b], Seok Gwon Jang [a,b], Van An Dinh [c], Bee Lyong Yang [a,b,*]

[a] *School of Advanced Materials Science and Engineering, Kumoh National Institute of Technology, 61 Daehak-ro, Gumi-si, Gyeongbuk 39177, the Republic of Korea*
[b] *GHS Co. Ltd., Gumi-Si, the Republic of Korea*
[c] *Department of Precision Engineering, Graduate School of Engineering, Osaka University, 2-1, Yamada-oka, Suita, Osaka 565-0871, Japan*

ARTICLE INFO

ABSTRACT

In this study, nickel-iron sulfide (NiFeS) nanosheets were immobilized on Ti$_3$C$_2$ MXene-decorated nickel foam (Ti$_3$C$_2$ MXene/NF) by hydrothermal reaction (NiFeS@Ti$_3$C$_2$ MXene/NF). The morphology of NiFeS and interactions with Ti$_3$C$_2$ MXene resulted in electronic coupling that optimized the adsorption energies of water, protons, and oxygen atom for the HER (180 mV@20 mA cm^{-2}) and OER (290 mV@20 mA cm^{-2}). The NiFeS@Ti$_3$C$_2$ MXene/NF catalyst showed good water splitting performance in an alkaline membrane water electrolyzer, yielding a current density (*j*) of 401 mA cm^{-2} at 1.85 V with 67.65 % cell efficiency, performance comparable to Pt/C||RuO$_2$ cells. From a commercial point of view, our electrolyzers are the best because of their low loading of catalysts (ca. 1.25 mg cm^{-2}) and low operating temperatures (50 °C), resulting in low capital and operating costs. Our findings will aid the development of commercial green hydrogen production and offers an alternative to PEMWE.

1. Introduction

The growing environmental concern resulting from the unchecked use of fossil fuels and energy shortages resulting population growth makes it necessary to develop renewable energy technologies [1,2]. Renewable-energy-driven water decomposition is a favorable path for the sustainable generation of hydrogen as an energy carrier, as well as the production of future green energy fuels [3,4]. The water decomposition process containing the oxygen and hydrogen evolution reaction (OER/HER); however, both the OER and HER are conventionally carried out using Ir, Ru and Pt catalysts, respectively [5]. However, the use of expensive precious metals is not practical when considering the large-scale commercialization of water electrolysis. Therefore, highly efficient, stable, and inexpensive catalysts for water electrolysis are required. To date, many non-precious metallic substances have been synthesized to serve as efficient electrocatalysts, such as nitrides [6,7], transition metal oxides [8,9], phosphides [7,10,11] sulfides [12,13], and selenides [14,15]. Among them, transition metal dichalcogenides

(TMDs) have been identified as a prime series of electrocatalysts showing high conductivities and being produced by easy-to-use manufacturing processes, making them promising for use in the development of superior electrocatalyst designs. Recently, a series layered TMDs based non-precious metal electrocatalysts such as Ni$_2$S, MoS$_2$, and FeS$_2$ have been reported for overall water decomposition [16]. The superior electrocatalytic activity of TMD catalysts for the OER and HER is a result of their unique structural properties, such as their structural disorder [17–19], doping with foreign metals [20] and morphology control [21,22]. Of these, nickel–iron based materials have received much more attention because of their low cost, high activity, and the synergistic coupling effect between nickel and iron compounds can enhance catalyst activity. For example, an Ni-FeS$_2$ lattice on Ni foams exhibit superior catalytic performance for the HER and OER [16].

Density function theory (DFT) calculation have shown that the electrocatalytic performance of TMDs can be further increased by binding to a conductive platform, which results in changes in ΔG_H^* and the electronic conductivity [23,24]. To this end, a number of catalysts

---

supports have been studied, such as multi-walled carbon nanotubes, reduced graphene oxide, and other carbon-based materials [25–28]. However, most such materials are hydrophobic and have very low electrochemical activities, which prevents their application in aqueous media. Therefore, to develop new materials having high catalytic performance, the identification of highly conductive, hydrophilic, and electrocatalytically active catalyst supports must be achieved.

Recently, MXene, a new class of metal carbides prepared by the exfoliation of MAX phases by selective etching, has drawn attention [29, 30]. The common formula of MXene is $M_{n+1}X_nT_x$ ($n = 1$–3), where M is a transition metal (Ti, Ta, Mo, and Nb), X is C, and T is the terminal functional group ($-O$, $-OH$, and/or $-F$). The Ti_3C_2 MXene is considered to be the most valuable candidate in the MXene family [31]. Owing to its special features, including a thin atomic layer, high electrical conductivity (Ti_3C_2; approximately 9880 S cm^{-1}), hydrophilicity, large number of active sites, and good mechanical properties, 2D Ti_3C_2 MXenes have been employed in various applications, including supercapacitors [32], batteries [30], water splitting [33,34], and biomedical applications [35]. Therefore, 2D Ti_3C_2 MXenes are a good choice of conductive catalytic support for tuning the overall catalytic water splitting reaction. For example, the MoS_2 growth on Ti_3C_2 MXene results in superior electrocatalytic performance because of the higher number of exposed MoS_2 edges and the lower ΔG_H* values [36].

Therefore, we propose an innovative approach to fabricating a synergistic hybrid heterostructured material by coupling the structural properties of Ti_3C_2 MXene with the vertically oriented growth of NiFeS nanosheets to achieve superior electrocatalytic components for overall water splitting. On the basis of earlier reports, we believe that the HER and OER activities of NiFeS can be increased by combining NiFeS and Ti_3C_2 MXene to create a NiFeS@Ti_3C_2 MXene hybrid structure.

In this study, we used easily reproducible electrochemical and hydrothermal methods to grow vertically oriented NiFeS on a layer of nickel (NF) foam containing Ti_3C_2 MXene. The obtained NiFeS@Ti_3C_2 MXene/NF catalyst showed higher catalytic activity towards HER and OER than those of NiFeS/NF and Ti_3C_2 MXene/NF. In particular, the NiFeS@Ti_3C_2 MXene/NF catalyst only showed overpotentials of 180 and 290 mV for the HER and OER, respectively, to obtain a current density (j) of 20 mA cm^{-2}. More importantly, the catalyst exhibited j of 10 mA cm^{-2} at 1.559 V and j of 401 mA cm^{-2} obtained at 1.85 V in a two-electrode cell and a zero-gap alkaline membrane water electrolyzer (AEMWE), respectively.

Overall, we found that the fine-tuning of the morphology and structure of NiFeS by its modification on the surface of Ti_3C_2 MXene on NF can affect the electron coupling between NiFeS and Ti_3C_2 MXene; specifically, the sulfur vacancies, which enhance electron transfer, resulting in an increase in the intrinsic HER and OER activities of the catalysts. Therefore, the current strategy to improve a catalyst for water splitting reaction offers the opportunity to manufacture high-quality TMD catalysts for electrochemical applications in the future.

2. Experimental

2.1. Materials

$FeCl_3$ $6H_2O$, $NiCl_2$ $2H_2O$, L-cysteine, KOH, HF, and CTAB were purchased from Alfa Aesar. Commercial RuO_2 (99.9 %) and Pt/C (20 wt%) were purchased (Sigma–Aldrich). Ti_3AlC_2 MAX (Nano shell, USA), Ni foam (MTI Korea, Ltd., thickness 1.5 mm, pore size: 500 μm), Sustain-ion™ X37–50 RT (Dioxide materials, USA), and Nafion® solution (5 wt %, Sigma–Aldrich) were also used. All materials and chemical were purchased without pretreatment. Deionized water was produced using a laboratory system (Millipore).

2.2. Synthesis method

2.2.1. Synthesis of Ti_3C_2 MXenes

1 g Ti_3AlC_2 powder was immersed in 100 mL HF solution and stirred for 48 h. Then, the mixed solution was neutralized by washing with water. Finally, Ti_3C_2 MXene was dried at 50 °C.

2.2.2. Preparation of Ti_3C_2 MXene/NF

Several pieces of NF with sizes of (1 cm^2) and (25 cm^2) were cut from a commercially available 3D-NF sheet, washed, and pretreated for experiments (for details, see Section S1 in the Supplementary Information (SI)). First, Ti_3C_2 was electrochemically deposited onto the NF electrode surface. Briefly, 200 mg Ti_3C_2 powder was dispersed in water (100 mL) by sonication for 30 min. Then, 10 mL of 0.1 M NaOH was used as a supporting electrolyte. Electrophoretic deposition was carried out in two-electrode H-type cell at 22 °C. Ni foam and Pt foil were utilized as the anode and cathode, respectively. The deposition of the Ti_3C_2 MXene was carried out by applying a voltage of 2 V for 30–60 s. During deposition, Ti_3C_2 MXene became coated to the Ni foam and stabilized by CTAB solution. The optimization of HER and OER activity as a function of deposition time (thickness) of Ti_3C_2 MXene is shown in Fig. S1.

2.2.3. Preparation of NiFeS@Ti_3C_2 MXene/NF

First, 0.05–0.15 mmol $NiCl_2$0.2 H_2O, 0.1–0.05 mmol $FeCl_3$0.6 H_2O, and L-cysteine (1 g)) were mixed in 30 mL water. Then, the above solution and NF samples were transferred into a 50-mL stainless-steel autoclave (Teflon-lined) and temperature was kept at 160 °C for 4 h. The NiFeS /NF composites were washed with water/ethanol mixture. The obtain products were dried at 60 °C for 10 h.

The probable reaction methods are given in Eqs. (1) and (2).

$$C_6H_{14}N_2O_4S_2 = NH_3 + CO_2 + H_2S \tag{1}$$

$$Ni + Fe + H_2S = Ni_2FeS_4 \tag{2}$$

The optimization of HER and OER activities as a function of the molar ratio of Ni and Fe in NiFeS is shown in Fig. S2, SI. A similar process was repeated to fabricate the optimized NiFeS@Ti_3C_2 MXene/NF electrode by taking the optimized composition of Ni and Fe. The catalyst load on the NF was approximately 1.25 mg cm^{-2}. Before electrochemical experiments, all electrodes were coated with 5 % Nafion® binder to achieve a loading of 0.25 mg cm^{-2} to prevent the mechanical loss of the catalysts during electrolysis. To prepare the NF electrode coated with commercial Pt/C and RuO_2 catalysts, a catalyst solution was dispersed by mixing the catalyst and 5 % Nafion® in ethanol. Finally, the catalyst was applied to the NF layer, and the catalyst loading was maintained at approximately 0.3 mg cm^{-2}.

2.3. Physical characterization techniques

The catalyst surface was evaluated using a field emission scanning electron microscope (FESEM, 10 kV/JSM-6500F, JEOL, Japan) and field emission transmission electron microscopy (FE-TEM; 200KV/JEM 2100F HR, JEOL, Japan). EDS (Energy Dispersive X-ray spectroscopy) measured the elemental mapping of the present catalyst (Jeol 6010, Japan). The Ni, Fe and Ti contents of the catalyst were determined by an Inductively Coupled Plasma Optical Emission Spectrometry (ICP-OES, Varian, 720-ES, UK). Internal structures, electronic states were investigated by X-ray diffraction (XRD; SWXD, Rigaku, Japan) and X-ray photoelectron spectroscopy (XPS, Thermo VG ESCALAB 250, USA), respectively. The BET surface area of the catalysts were analyzed on a N_2 adsorption analyzer (Flex & 3Flex, USA).

2.4. Electrochemical measurement techniques

All electrochemical measurements for HER and OER evaluation were performed with the studied catalyst by a three-electrode arrangement in

Ar-saturated 1 M KOH solution at 22 °C. A catalyst-coated nickel foam (1 cm × 1 cm, NF) was taken as the working electrode, and an Ag/AgCl electrode was utilized as the reference electrode in an alkaline electrolyte. To complete the three-electrode circuit system, a graphite rod and Pt foil were utilized as counter electrodes for both HER and OER, respectively. NF coated with RuO$_2$ and 20 % Pt/C with Nafion® binder were used as commercial OER and HER catalysts, respectively, for comparison. The HER/OER activity was evaluated by linear sweep voltammetry (LSV) using an electrochemical workstation (AMT VERSTAT3, USA) at a scan rate of 10 mV s^{-1}. The obtained potential values were converted to the reversible hydrogen electrode (RHE) scale according to the equation E(RHE) AgCl = E(vs. Ag/AgCl) + E^0(Ag/AgCl) + 0.0592 × pH. Polarization curves were collected after *iR* correction in 1 M KOH solution. The linear part of the Tafel plot was fitted to the Tafel equation = $a + b \log(j)$ and the Tafel slope b was obtained. Electrochemical impedance spectroscopy (EIS) was analyzed over the frequency range of 1 Hz to 1 MHz. Details of the electrochemical measurement techniques are given in Section S2 in SI.

2.5. DFT calculation

The spin-polarized density functional theory was employed using Vienna Ab Initio Simulation Package (VASP) [37,38], within the generalized gradient approximation of Perderw, Burke, and Ernzerhof (GGA-PBE) formulation [39]. The ionic cores and valence electrons were treated by the projector augmented wave (PAW) method [40]. An energy cutoff of 500 eV was used for the plane-wave basis set. All structures were relaxed by full optimization. The Γ-centered 3 × 3 × 1 k-point grids were used for Ti$_3$C$_2$ MXene and NiFeS, while the Γ-centered 2 × 2 × 1 k-point grids were sampled for the NiFeS@Ti$_3$C$_2$ MXene hybrid. A vacuum of 15 Å was included to avoid interaction between the periodical slabs. The force convergence for structural relaxation was chosen at 0.04 eV/Å. In addition, the van der Waals interaction was also considered using Grimme DFT-D3 methodology [41]. Details of DFT calculations are given in Section S3, SI.

2.6. Alkaline water electrolyzer setup and experimental conditions

2.6.1. Conventional two-electrode electrolyzer

The electrolyzer cell was prepared from a homemade single compartment cell. The NiFeS@Ti$_3$C$_2$ MXene fabricated Ni foam (5 cm × 5 cm) was used as anode and cathode. For comparison, a water electrolyzer was assembled by integrating the Pt/C/NF (cathode) and RuO$_2$/NF (anode) under similar experimental conditions and mass loading (0.3 mg cm^{-2}).

2.6.2. Commercial zero-gap anion exchange membrane electrolyzer

An anion-exchange membrane was utilized as the solid polymer matrix in the water electrolysis test. The membrane was activated before electrolysis to remove water-soluble materials from the structure and activate the ion-exchange particles. Details of the membrane activation process are described in Section S4 in the SI.

An anion-exchange membrane (Sustainion™ X37–50 RT) was sandwiched between two NiFeS@Ti$_3$C$_2$ MXene/Ni foam electrodes (cathode and anode) by hot press method (40 °C, 2 MPa) to prepare the membrane electrode assembly (MEA). The nickel (gold plated) was used as the end plate and current collector. The thus-prepared single anion-exchange membrane water electrolyzer (AEMWE) cell was operated at 50 °C using a 1 M KOH aqueous medium. The electrolyzer activity was determined by the load curve at applied potential of 1.5–2.0 V. Stability of the elecrolyzer performance was evaluated under AEMWE conditions at a constant applied potential. For comparison, MEAs containing a Pt/C/NF cathode and a RuO$_2$/NF anode with a mass load (0.3 mg cm^{-2}) were constructed and tested under similar experimental conditions.

3. Result and discussion

3.1. Morphology and phase analysis

Our easily reproducible procedure for preparing the NiFeS@Ti$_3$C$_2$ MXene/NF electrode is posted in Fig. 1a. In the first step, Ti$_3$C$_2$ MXene was electrochemically decorated on a three-dimensional NF layer. FESEM characterization revealed that the three-dimensional (3D) rough surface of the NFs was smooth after the deposition of Ti$_3$C$_2$ MXene. Fig. 1b and the inset show the SEM images of NF and Ti$_3$C$_2$ MXene/NF showing this modification. Finally, the vertical growth of NiFeS on Ti$_3$C$_2$ MXene/NF surfaces was achieved by the hydrothermal method with L-cysteine as the sulfur source (Fig. 1c and S3). The EDS analysis of NiFeS@Ti$_3$C$_2$MXene/NF revealed the presence of Ti, C, Ni, Fe, and S (Figs. S3–4). The Ni, Fe and Ti contents of NiFeS@Ti$_3$C$_2$ MXene/NF were measured by ICP-OES (Inductively Coupled Plasma Optical Emission Spectrometry) and posted in Table S1. The ICP-OES results support EDS data.The XRD pattern of the NiFeS@Ti$_3$C$_2$ MXene/NF electrode is illustrated in Fig. 1d. The pattern shows XRD peaks located at 44.65°, 51.94°, and 76.51°, corresponding to the (111), (200), and (220) planes, respectively, of metallic Ni (JCPDS card no. 04–850), 6.9°, 17.4°, 29.1°, 38.3°, 43.5°, and 62.5° corresponding to the (002), (004), (006), (008), (010), and (110) planes, respectively, of Ti$_3$C$_2$ MXene [42,43], and 12.5°, 21.7°, 32.4° 37.1°, 47.2°, 50.1, and 55.6° corresponding to (111), (220), (311), (400), (422), (533), and (440) planes, respectively, of cubic thio-spinel structure of Ni$_2$FeS$_4$ (ICOD No. 00–047–1740) [44]. XRD analysis confirmed the hybrid structure of Ti$_3$C$_2$ MXene and Ni$_2$FeS$_4$ on the NF layer. In Fig. 2a, the FETEM image shows that the NiFeS nanosheets aggregated to form flower-like structures. The HRTEM images coupled with fast Fourier transform (FFT) pattern posted in Fig. 2b and c reveal the presence of lattice fringes of 0.236 and 0.144 nm, represents to the (400) and (533) patterns of Ni$_2$FeS$_4$, respectively, and a spacings of 0.250 nm corresponding to the (006) pattern of MXene [45–47]. In Fig. 2c, S vacancies (V$_S$) can be observed, and these should increase the electron density of Ni and Fe and enhance the HER and OER kinetics. The TEM image coupled with EDS mapping show the presence of Ti, C, Ni, Fe, and S, confirming the hybrid structure of the NiFeS@-Ti$_3$C$_2$ MXene (Fig. 2d). The BET surface area was measured to be ~19.8 m^2 g^{-1} for NiFeS@Ti$_3$C$_2$/NF, posted in Fig. S5. This is in good correlation with the SEM images.

Next, the electronic and chemical nature of the elements in the NiFeS@Ti$_3$C$_2$ MXene catalysts were examined by XPS. XPS full spectrum shown in Fig. S6a indicates the presence of Ni, Fe, Ti, S, and C. The Ti 2p high-resolution spectrum is shown in Fig. S6b. In this spectrum, the contributions of C and O can be presented to TiC and TiO$_x$, respectively. Furthermore, the peak positions at 454.9 (sp^3) and 461.2 eV (sp^1) confirms the contribution from the Ti-C bonds, whereas the peak positions at 456.6 and 462.7 eV represent to the Ti-O bonds [48,49]. The high-resolution C 1 s XPS spectrum of NiFeS@Ti$_3$C$_2$ MXene can be fitted into four peaks at 282.5, 284.5, 284.9, and 287.1 eV, represents to C–Ti, C–Ti–C, C–C, and C–OH bonds (Fig. S6c) [42,49]. The Ni 2p spectra contain peaks that can be fitted into two doublets having two satellite peaks at 855.9 and 873.4 eV, assigned to 2p$_{3/2}$ (Ni^{3+}) and 2p$_{1/2}$ (Ni^{3+}), respectively, as shown in Fig. S6d. The increase in the Ni^{3+} peak intensity indicates the formation of the Ni$_2$FeS$_4$ phase [44]. In Fig. S6e, at binding energies of 724.0 and 710.8 eV, the two main peaks were assigned to Fe 2p$_{1/2}$ and Fe 2p$_{3/2}$, respectively. The characteristic of Fe 2p$_{3/2}$ spectra are 713.5 (Fe(III)–S) and 715.7 eV (Fe(II)– S) [50]. In addition, the two satellite peaks indicate hydride systems of Fe^{2+} and Fe^{3+}. In the S 2p spectra in Fig. S6f, the peaks are divided into two peaks (162.2 and 163.5 eV), which can be attributed to S 2p$_{1/2}$ and S 2p$_{3/2}$ and are characteristic of S^{2-} of Ni$_2$FeS$_4$ [50–52]. The shift of binding energy to the higher energy level represents the electron transfer from S to Ni and Fe atoms induced by the presence of sulfur vacancies [53,54]. These results indicate that the electronic structures of Ti, Fe, and Ni were altered by the presence of strong covalent interactions between NiFeS
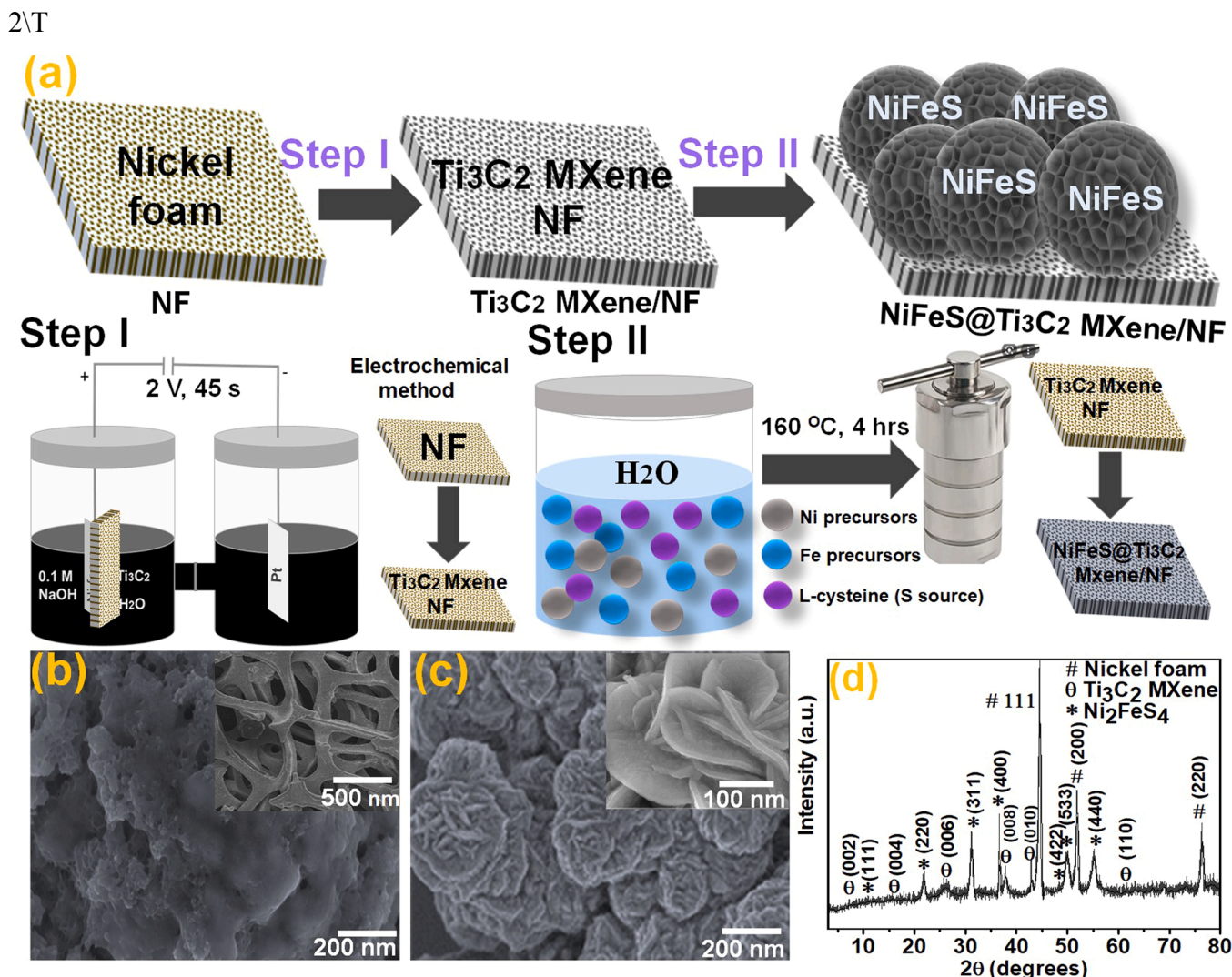
2\T

Fig. 1. (a) Schematic presentation of NiFeS@Ti₃C₂ MXene/NF electrode preparation method. SEM images of (b) Ti₃C₂ MXene/NF and NF (inset) and (c) NiFeS@Ti₃C₂ MXene/NF. (d) XRD pattern of NiFeS@Ti₃C₂ MXene/NF.

and Ti₃C₂ MXene, and, further, the heterogeneous interfacial electronic coupling could promote the HER activity [55].

3.2. Catalytic activity

3.2.1. HER activity evaluation

To analyze the HER activity of the present catalysts, we evaluated the LSV curve at a scan rate of 10 mV s^{-1}. The polarization curve in Fig. 3a shows a dependent behavior.

As shown in Fig. 3b, the overpotential required to achieve the j of 20 and 50 mA cm^{-2} for Ti₃C₂ MXene/NF, NiFeS/NF, NiFeS@Ti₃C₂ MXene/NF and 20 % Pt/C catalysts is 320 and 550, 250 and 350, 180 and 320, 150 and 280 mV, respectively.

In Fig. 3c, the Tafel slopes of NF, Ti₃C₂ MXene/NF, NiFeS /NF, NiFeS@Ti₃C₂ MXene/NF, and 20 % Pt/C were 270, 240, 210, 177, and 165 mV dec^{-1}. Remarkably, the NiFeS@Ti₃C₂ MXene/NF catalysts yielded a comparable Tafel slope (177 mV dec^{-1}) to close the Pt/C catalyst (165 mV dec^{-1}) at lower potentials, as well as faster H₂ production on the application of a potential, proposed that the HER over this catalyst shows the Volmer–Tafel reaction steps.

$$M^* + H_2O + e^- = M^*H_{ad} + OH^- \text{ (Volmer reaction)} \quad (3)$$

$$M^*H_{ad} + H_2O + e^- = H_2 + M^* + OH^- \text{ (Heyrovsky)} \quad (4)$$

$$2 M^*H_{ad} = H_2 + M^* \text{ (Tafel)} \quad (5)$$

The high HER activity of the NiFeS@Ti₃C₂ MXene/NF electrode can be explained using the water adsorption (ΔG_{H2O}^*) and H* adsorption and desorption (ΔG_H^*) energies. According to previous studies, a negative ΔG_{H2O}^* for a catalyst indicates a thermodynamically favorable Volmer step [56].

Electrochemical impedance spectroscopy (EIS) data are illustrated in Fig. 3d, showing that the NiFeS@Ti₃C₂ MXene/NF electrode exhibits a smaller semicircle compared to the other counter electrodes (NiFeS/NF and Ti₃C₂ MXene/NF). The smaller semicircle confirms low HER charge transfer resistance and faster reaction kinetics. However, in this work, the apparent electrcatalytic activity of the catalyst was studied in terms of the TOF, which was calculated based on the Charge (Q) of the electron transfer to the active ion of the catalysts [57] (see the Fig. 3e and Sections S5–6 in SI). In Fig. 3e, the HER TOF (at an overpotential of 300 mV) of the NiFeS@Ti₃C₂ MXene/NF and NiFeS@Ti₃C₂ MXene/NF catalysts were 0.13 and 0.41 s^{-1}, respectively.

The electrochemically active surface area (ECSA) was analyzer (details Section S7 and Fig. S7 in SI). NiFeS@Ti₃C₂/NF exhibits a higher ECSA (~262 cm^{-2}) and is 1.4 times more than that of NiFeS/NF (~187 cm^{-2}). Therefore, the coupling between NiFeS and Ti₃C₂ can
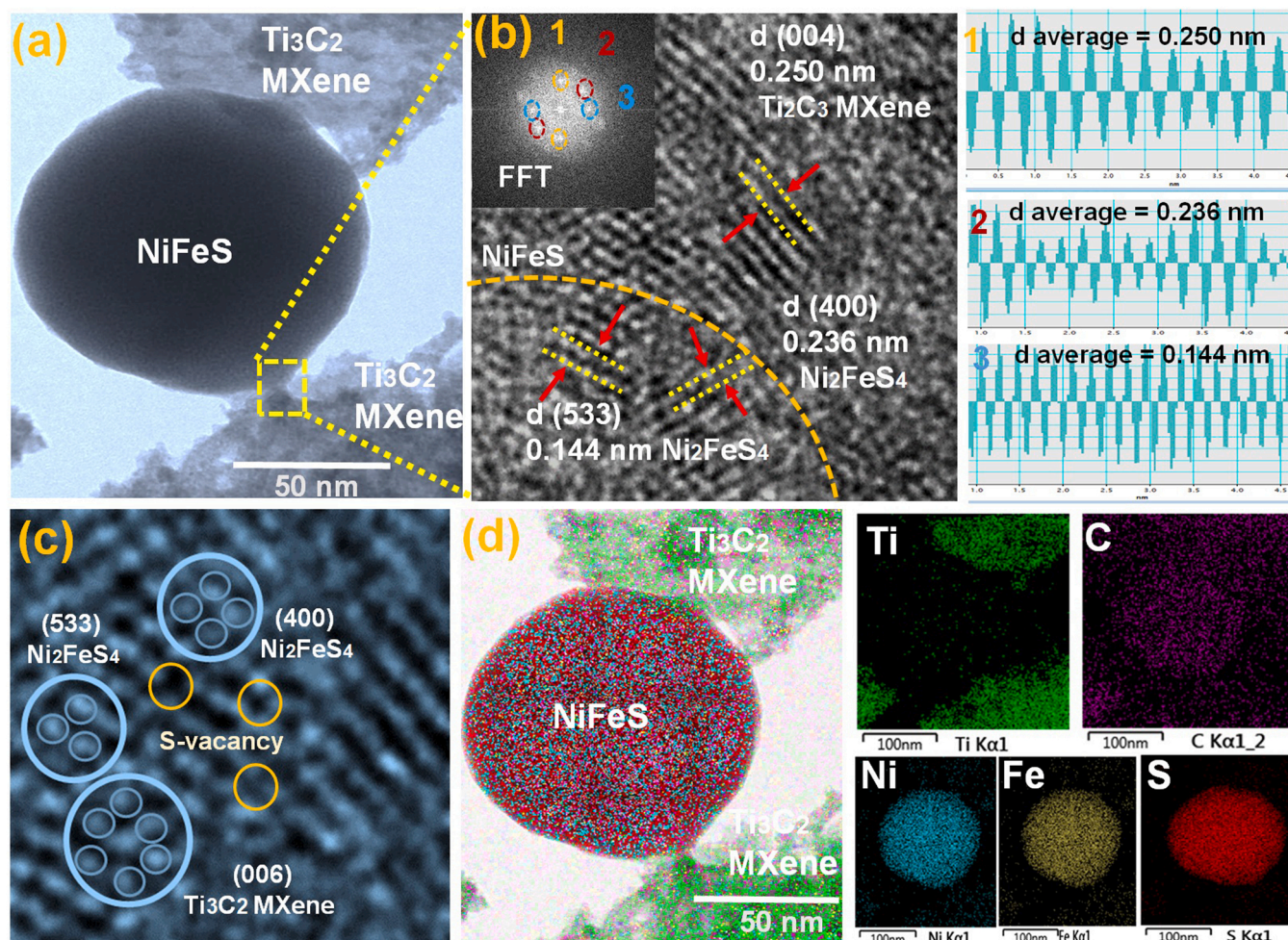
2\T

Fig. 2. TEM image of (a) NiFeS@Ti$_3$C$_2$ MXene/NF and the corresponding (b) HRTEM image with fast Fourier transform (FFT) in the inset. (c) Atomic arrangements of NiFeS and Ti$_3$C$_2$ MXene and sulfur vacancies. (d) TEM-EDS elemental maps of NiFeS@Ti$_3$C$_2$ MXene/NF.
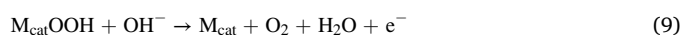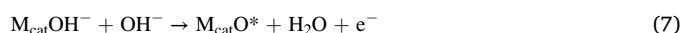
significantly increase the ECSA, promoting better charge transfer process.Notably, the hybrid structure of NiFeS with Ti$_3$C$_2$ MXene results in superior HER activity, possibly because the highly conductive Ti$_3$C$_2$ MXene confirm the formation of an active reaction phase during the reversible oxidation of nickel iron sulfide to nickel iron oxy-sulfide, thus facilitating charge transfer and improving the HER kinetics [36,46]. Finally, the HER durability of the NiFeS@Ti$_3$C$_2$/NF electrode was investigated by chronopotentiometry measurements over 24 h. In Fig. 3f, the NiFeS@Ti$_3$C$_2$ MXene/NF electrode stability tests were conducted at j of 20 and 50 mA cm^{-2}. The stability tests indicated that the catalysts showed sufficient HER stability, having negligible decay rates of 0.45 % and 0.99 % at 20 and 50 mA cm^{-2}, respectively. In Fig. S8, continuous cyclic voltammetry diagrams for HER stability test support this result.

3.2.2. OER activity evaluation

To evaluate the OER activity of the prepared catalysts with respect to commercial RuO$_2$, LSV curves were obtained at a scan rate of 10 mV s^{-1} (Fig. 4a), and the overpotentials of all catalysts needed to obtain j of 20 and 50 mA cm^{-2} were obtained as a metric of catalyst performance. As shown in Fig. 4b, NiFeS@Ti$_3$C$_2$ MXene/NF required the lowest overpotentials of 276 and 320 mV to obtain the j of 20 and 50 mA cm^{-2}, respectively. However, NiFeS@Ti$_3$C$_2$ MXene/NF yielded lower overpotentials than NiFeS/NF (300 mV@20 mA cm^{-2} and

360 mV@50 mA cm^{-2}), Ti$_3$C$_2$ MXene/NF (360 mV@20 mA cm^{-2} and 450 mV@50 mA cm^{-2}), and NF (370 mV@20 mA cm^{-2} and 470 mV@50 mA cm^{-2}). Thus, our catalysts had similar activities to that of the RuO$_2$ catalyst (280 mV@20 mA cm^{-2} and 355 mV@50 mA cm^{-2}). Next, the Tafel slope was obtained to provide a further understanding of the kinetics of the OER process. In particular, we identified the four-electron-transfer rate-determining steps (RDS), as shown in Fig. 4c. The obtained OER Tafel slopes for NF, Ti$_3$C$_2$ MXene/NF, NiFeS/NF, NiFeS@Ti$_3$C$_2$ MXene/NF, and RuO$_2$/NF were 75, 72, 59, 45, and 34 mV dec^{-1}, respectively. The low Tafel slope and overpotential indicate that NiFeS@Ti$_3$C$_2$ MXene/NF exhibits fast OER kinetics corresponding to very high OER activity.

According to the literature, the OER of metal chalcogenides follows the following fundamental reaction steps [58], as given by Eqs. (6)–(9).

$$M_{cat} + OH^- \rightarrow M_{cat}OH + e^- \tag{6}$$

$$M_{cat}OH^- + OH^- \rightarrow M_{cat}O^* + H_2O + e^- \tag{7}$$

$$M_{cat}O^* + OH^- \rightarrow M_{cat}OOH + e^- \tag{8}$$

$$M_{cat}OOH + OH^- \rightarrow M_{cat} + O_2 + H_2O + e^- \tag{9}$$

The Tafel slope obtained was close to 60 mV dec^{-1}, demonstrates that the RDS is the reaction in Eq. (8).

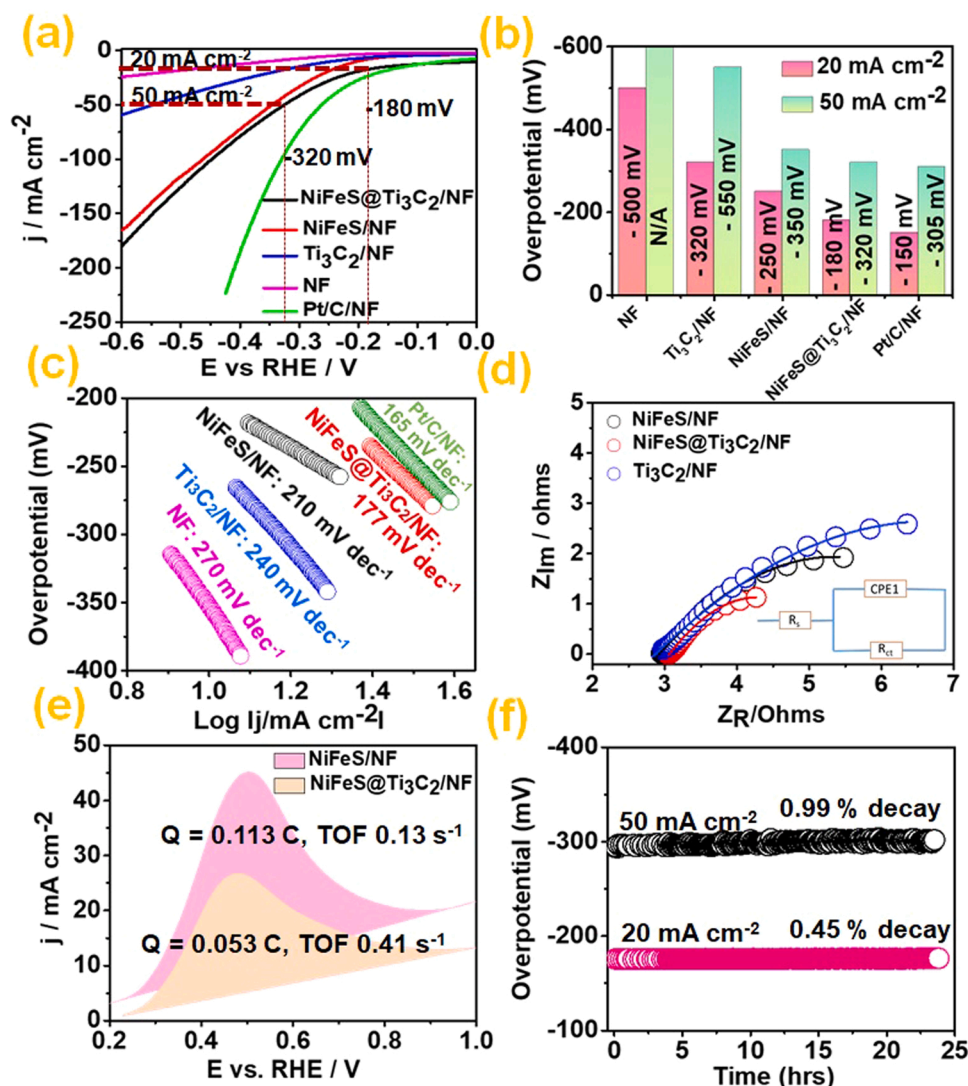The TOF of NiFeS@Ti$_3$C$_2$ MXene/NF was 0.11 s^{-1}, clearly indicating

2\T

Fig. 3. (a) Polarization curves showing the HER evaluation of the catalysts and (b) overpotentials of all electrodes at j of 20 and 50 mA cm^{-2}. (c) Tafel slopes of the studied electrodes. (d) EIS spectra at an overpotential of 200 mV. (e) Coulombic charge area and calculated turnover frequency (TOF). (f) Chronopotentiometric measurements over 24 h for stability testing of the NiFeS@Ti$_3$C$_2$ MXene/NF electrode at constant j of 20 and 50 mA cm^{-2}. Experimental conditions: Ar-saturated 1 M KOH, 22 °C and catalyst loading of approximately 1.25 mg cm^{-2} and a Pt/C loading of approximately 0.3 mg cm^{-2}.

the higher OER catalytic activity compared to that of the base electrode, i.e., NiFeS/NF (0.046 s^{-1}). For details, see the Section S8 in SI. The superior OER activity of the NiFeS@Ti$_3$C$_2$ MXene/NF electrode could be attributed to show the lower charge transfer resistance (R_{ct}), as shown by the EIS spectra in Fig. 4d. In particular, the EIS spectra contain a smaller semicircle for NiFeS@Ti$_3$C$_2$ MXene/NF than those of the NiFeS/NF and Ti$_3$C$_2$ MXene/NF electrodes. These results demonstrate that Ti$_3$C$_2$ MXene results in increased conductivity, possibly as a result of the intimate electrical contact between NiFeS@Ti$_3$C$_2$ MXene and the NF; this reduces R_{ct} and improves the OER kinetics. To verify the stability of the NiFeS@Ti$_3$C$_2$ MXene/NF electrode catalyst for the OER, chronopotentiometry analysis was performed at j of 20 and 50 mA cm^{-2} (Fig. 4e). The durability tests revealed that the NiFeS@Ti$_3$C$_2$ MXene/NF exhibited efficient stability with minimum decay rates of 0.82 % (20 mA cm^{-2}) and 1.5 % (50 mA cm^{-2}), respectively. In Fig. S9, continuous cyclic voltammetry diagrams for OER stability test support this result.

In addition, the NiFeS@Ti$_3$C$_2$ MXene/NF electrode exhibited low cathode and anode overpotentials of 180 (20 mA cm^{-2}) and 290 mV (20 mA cm^{-2}), respectively. As shown in Fig. 4 f, the overpotential value of NiFeS@Ti$_3$C$_2$ MXene/NF is much lower than that of the recently published catalysts such as CoP@ 3D MXene (220 mV/300 mV) [59], Ni$_{0.7}$Fe$_{0.3}$PS$_3$ @MXene (240 mV/300 mV) [60], NiFe$_2$O$_4$/Ti$_3$C$_2$ (230 mV/310 mV) [33],

TiN@NiO-NiSe$_2$ (190 mV/305 mV) [61], Ni$_x$Co$_{3-x}$O$_4$/Ti$_3$C$_2$T$_x$-HT (260 mV/330 mV) [62], and NiFe$_2$O$_4$/Ti$_3$C$_2$ (220 mV/296 mV) [33] and has a similar overpotential to those of MXene-NiCoP (175 mV/280 mV) [63], Co-CoO/Ti$_3$C$_2$-MXene/NF (110 mV/295 mV) [64], NiFe-LDH@-Mo–NiS$_2$–NiS/NF (170 mV/291 mV) [65], Ni$_2$P@FePOx (105 mV/240 mV) [66], Fe-CoP/NF (170 mV/220 mV) [67], and MoS$_2$/NiFe-LDH (210 mV/220 mV) [68]. Further, we analyzed the surface of the catalyst by FESEM and FETEM after 24 h of HER and OER tests. Shown in Fig. S10, the FESEM and FETEM images show that the nanosheet structure remained unchanged after the experiment, confirming the stability of the catalyst and its potential for use in practical electrolyzer applications. In addition, XPS analysis of the electrodes before and after HER/OER experiments demonstrated the structural stability of the catalyst (Fig. S11).

3.2.3. DFT results and discussion

To better to understand the underlying mechanism of HER and OER for NiFeS@Ti$_3$C$_2$ MXene, we investigated density functional theoretical (DFT) calculations. According to our experimental condition and some previous studies [56,69], we constructed the Ni$_2$FeS$_4$ supported by O-terminated Ti$_3$C$_2$ (NiFeS@Ti$_3$C$_2$ MXene), Ni$_2$FeS$_4$ (NiFeS) and O-terminated Ti$_3$C$_2$ (Ti$_3$C$_2$ MXene) models (Fig. 5a). The total density of states (TDOS) of all models are calculated and displayed in Fig. 5b. Obviously, the electron density around Fermi level of NiFeS@Ti$_3$C$_2$
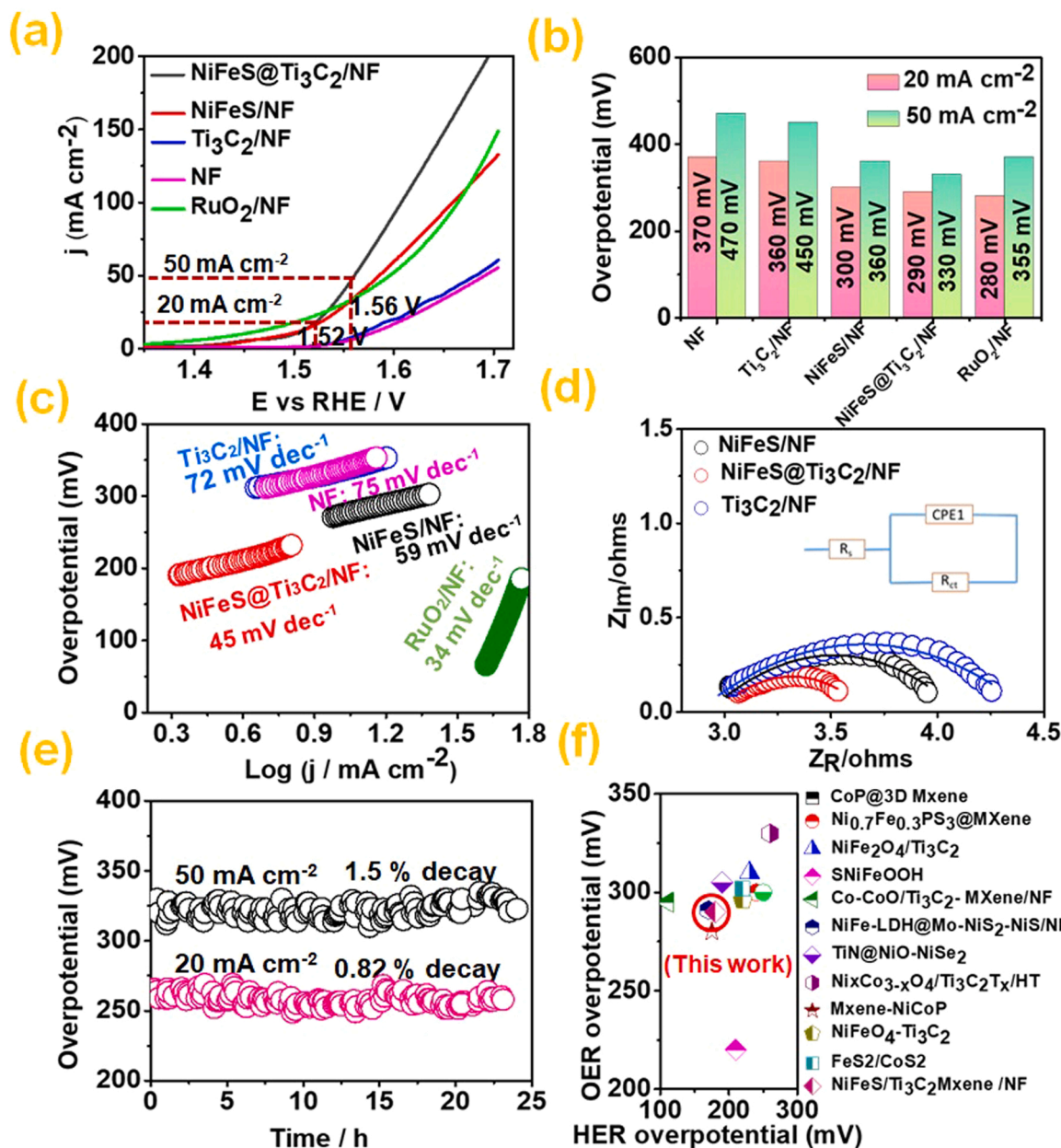
2\T

Fig. 4. (a) Polarization curves for the OER and (b) overpotentials of all electrodes at *j* of 20 and 50 mA cm^{-2}. (c) Tafel slopes of all studied electrodes. (d) EIS spectra of the studied electrodes at an overpotential of 200 mV. (e) Chrono potentiometric stability tests of the NiFeS@Ti$_3$C$_2$ MXene/NF electrode over 24 h at constant *j* of 20 and 50 mA cm^{-2}. (f) Comparison of the obtained HER/OER activities with previously reported results. Experimental conditions: Ar-saturated 1 M KOH, 22 °C, catalyst loading of approximately 1.25 mg cm^{-2}, and RuO$_2$ loading of approximately 0.3 mg cm^{-2}.

MXene is higher than that of NiFeS and Ti$_3$C$_2$ MXene, implying the enhanced electrical conductivity and charge/electron transfer, thus facilitating the adsorption/desorption of intermediates and reducing the intrinsic kinetic barriers. Generally, the Gibbs free energy of hydrogen adsorption (ΔG_{H^*}) is still a vital descriptor to predict the HER activity of electrocatalysts [70,71]. To achieve the optimized hydrogen adsorption/desorption, the $|\Delta G_{H^*}|$ value is expected to be as small as possible. In Fig. 5c, the ΔG_{H^*} value of NiFeS@Ti$_3$C$_2$ MXene is found to be 0.03 eV, which is slightly lower than that of NiFeS (0.07 eV) and Ti$_3$C$_2$ MXene (−0.47 eV). To identify actual active centers in NiFeS@Ti$_3$C$_2$ MXene, we investigated the various possible adsorption sites on NiFeS@Ti$_3$C$_2$ MXene surface. The ΔG_{H^*} values of 0.03, 0.49 and 0.68 eV are observed for S-site, Ni-site and Fe-site, respectively, indicating the S atoms in the NiFeS@Ti$_3$C$_2$ MXene are taken into account for the improvement of HER

activity (Fig. 5d). Fig. 5e shows the Gibbs free energy of OER at an equilibrium potential of 0 V. Notably, the OER RDS of MXene is the first formation of *OH with the free energy barrier of 2.85 eV, while the RDS of NiFeS@Ti$_3$C$_2$ MXene and NiFeS is the formation of *OOH from *O with free energy barriers of 1.94 and 2.15 eV, respectively. The lower RDS value of NiFeS@Ti$_3$C$_2$ MXene exhibits that the formation energy of O−O band can be reduced by the synergistic effect of NiFeS and Ti$_3$C$_2$ MXene [72]. Specifically, the theoretical OER overpotentials of NiFeS@Ti$_3$C$_2$ MXene, NiFeS and Ti$_3$C$_2$ MXene are calculated to be 0.71, 0.92 and 1.62 V, respectively, favoring the balance between adsorption and desorption intermediates in NiFeS@Ti$_3$C$_2$ MXene. The OH* adsorption energy (ΔG_{OH^*}) is strongly dependent on the surface electronic structure, such as the presence of sulfur vacancy (V_S), having strong adsorption energies of at vacancy sites. Crucially, the presence of
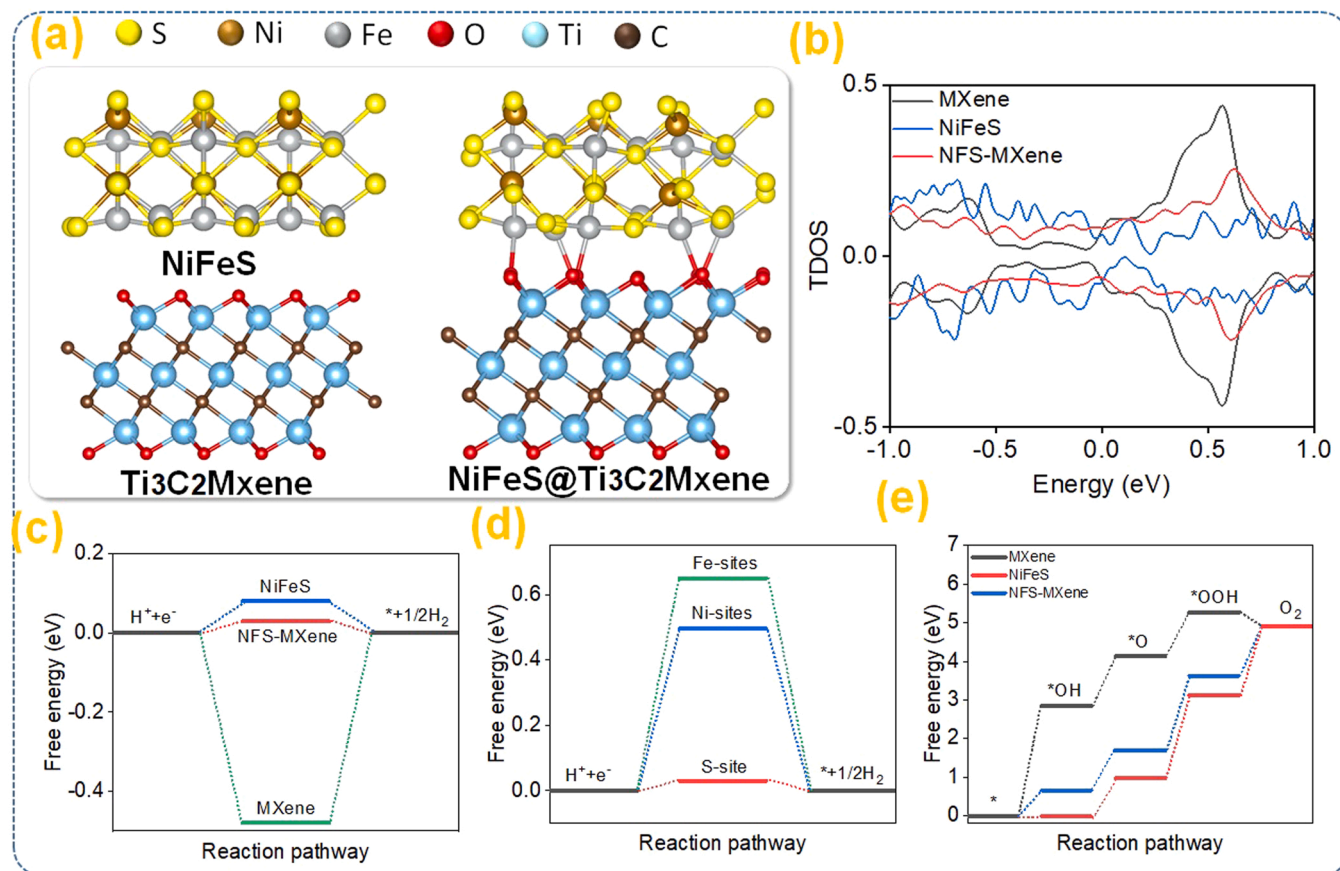
2\T

Fig. 5. (a) Slab model of NiFeS@Ti$_3$C$_2$ MXene; (b) Total density of states (TDOS) values of NiFeS, Ti$_3$C$_2$ MXene and NiFeS@Ti$_3$C$_2$ MXene with fermi level; (c) Gibbs –free energy for HER kinetic of NiFeS@Ti$_3$C$_2$ MXene; (d) ΔG$_{H*}$ values profile for S-site, Ni-site and Fe-site of NiFeS; (e) Gibbs –free energy for HER kinetic of NiFeS@Ti$_3$C$_2$ MXene.

V$_S$ can shift the center of the ᴅ-band to a lower energy, resulting in decreased M-O* and M-OOH binding energies and enhanced OER kinetics [73,74]. In summary, these theoretical results further prove that the electronic coupling between NiFeS and Ti$_3$C$_2$ MXene exhibits suitable binding affinities towards HER/OER reaction intermediates and synergistically reduces the kinetic barriers.

The excellent bifunctional performance of the NiFeS/Ti$_3$C$_2$ MXene/ NF electrode can be illustrated by the following factors.

1. The interfacial electronic coupling facilitates electron transfer and effectively promotes the electrocatalytic activity of NiFeS/Ti$_3$C$_2$ MXene for the alkaline hydrogen and oxygen evaluation kinetics. In addition, modulating the electronic structure of NiFeS and Ti$_3$C$_2$ MXene results in appropriate M-H and M-O bond energies for better electrocatalytic HER and OER kinetics.
2. The weak van der Waals interaction between the Ti$_3$C$_2$ MXene and NiFeS nanosheets promotes the exposure of more active catalytic sites and creates an effective reaction domain that can increase the catalytic activity.
3. The synergistic interaction between the thin lamellar structure of Ti$_3$C$_2$ MXene and the nanosheet structure of NiFeS improves the structural integrity of the hybrid material and facilitates ion transport for better HER and OER performance.
4. Structural defects can change the electrochemical properties of catalysts, leading to new strategies for catalyst growth. The resulting hybrid structure has more internal channels for the transport of ions/ electrons and generates more active sites for the HER and OER.

5. Sulfur vacancies can promote the OER by increasing the electron density of Ni and Fe. Furthermore, density functional theory calculations have demonstrated that Ti$_3$C$_2$ MXene can activate the S sites of NiFeS and, thus, enhance the OER kinetics [23].

3.3. Alkaline water electrolysis performance

3.3.1. Conventional two-electrode electrolyzer performance

The practical application of NiFeS@MXene/NF in an overall-water splitting system was tested using a lab-made one-chamber electrolyzer, in which the NiFeS@Ti$_3$C$_2$ MXene/NF electrodes act as anode and cathode GDL (Fig. 6a). The current–potential curve obtained from the test showed that the electrolyzer had a high j, reaching 10 mA cm^{-2} at a cell potential of 1.559 V. Moreover, at voltage of 1.842 V, the obtained j was 50 mA cm^{-2}; this voltage is substantially lower than those of the other catalysts (NiFeS/NF, Ti$_3$C$_2$ MXene/NF, and NF). More importantly, the j of the NiFeS@Ti$_3$C$_2$ MXene/NF(+)||NiFeS@Ti$_3$C$_2$ MXene/ NF(-) cell at 1.95 V is approximately 1.5-times more j than Pt/C||RuO$_2$, resulting the catalytic performance under overall water splitting conditions. In addition, the electrolyzer test indicated that the NiFeS@Ti$_3$C$_2$ MXene/NF electrode showed similar trends in activity to the catalyst three-electrode testing results (Fig. 6b). Thus, next, the stability of the electrolyzer was investigated using constant j at 10 and 50 mA cm^{-2}.

As shown in Fig. 6c, the electrolyzer provided a j of 10 mA cm^{-2} with a minimum decay rate of 0.78 % and j of 50 mA cm^{-2} with a minimum decay rate of 1.7 % over 90 h of long-term operation. These results confirmed the negligible loss of the catalysts and suggest their promise for commercial applications. The H$_2$ and O$_2$ bubbles formed at the anode
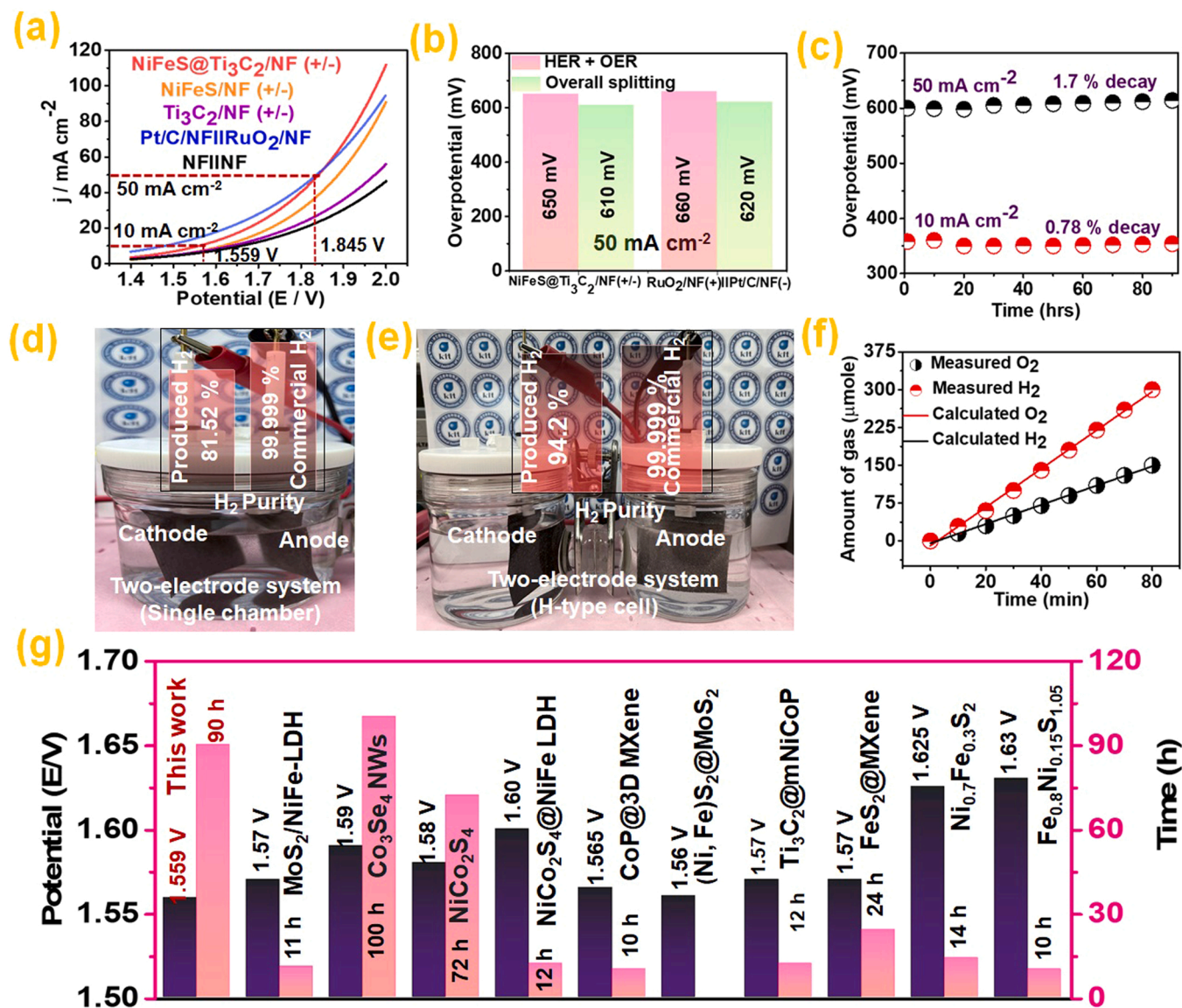
2\T

Fig. 6. (a) I-V load curves for overall water splitting using all electrodes. b) Overall overpotentials of the two-electrode and three-electrode systems. (c) Chrono potentiometric stability testing of the NiFeS@Ti$_3$C$_2$ MXene/NF electrode over 24 h at constant *j* of 10 and 50 mA cm^{-2}. (d) Photo of single chamber electrolyzer. (e) Photo of H-type electrolyzer. (f) Amount of H$_2$ production with time (g) Comparison with previous results. Experimental conditions: 1 M KOH, 22 °C, catalyst loading of approximately 1.25 mg cm^{-2}, Pt/C loading of approximately 0.3 mg cm^{-2}, and RuO$_2$ loading of approximately 0.3 mg cm^{-2}.

and cathode, respectively, were next analyzed for purity by gas chromatography (GC).

The purity of the generated H$_2$ gas was 81.52 % (Fig. 6d, photo of H$_2$ and O$_2$ evaluation, single chamber two-electrode system, details in Video 1), which is significantly lower than that of commercial hydrogen (99.999 %). In contrast, the purity of the H$_2$ produced in the H-type cell was 94.2 % (Fig. 6e, H-type two-electrode system, details in Video 2). In addition, the H$_2$ and O$_2$ gas produced were measured quantitatively. Fig. 6f shows the volumes of H$_2$ and O$_2$ evolved with time and a comparison of the experimentally obtained and theoretical gas volumes. Clearly, the volumetric ratio (molar) of H$_2$ and O$_2$ is close to 2 (0.345 mL/min):1 (0.17 mL/min), indicating almost 98.9 % faradaic efficiency (section S9 in SI). Therefore, for the production of 99.999 % pure hydrogen, the zero-gap membrane water electrolyzer is a viable option for hydrogen production.

Supplementary material related to this article can be found online at doi:10.1016/j.apcatb.2022.122039.

In Fig. 6 g, a comparison of these results with those of recently published catalysts is shown: MoS$_2$/NiFe-LDH (+/-) @ 1.57 V, 11 h [75]; Co$_3$Se$_4$ NWs (+/-) @ 1.59 V, 100 h [76]; NiCo$_2$S$_4$ (+/-) @ 1.58 V, 72 h [77]; NiCo$_2$S$_4$ @NiFe LDH (+/-) @ 1.60 V, 12 h [78]; CoP@ 3D Ti$_3$C$_2$-MXene (+/-) 1.565 V, 10 h [59]; (Ni, Fe)S$_2$ @MoS$_2$ (+/-) 1.56 V [79]; Ti$_3$C$_2$ @mNiCoP (+/-) 1.57 V, 12 h [63]; FeS$_2$ @MXene (+/-) 1.57, 24 h [80]; Ni$_{0.7}$Fe$_{0.3}$S$_2$ (+/-) 1.625 V, 14 h [81]; and Fe$_{0.8}$Ni$_{0.15}$S$_{1.05}$ 1.63 V, 10 h [51]. Comparing these values, our NiFeS@Ti$_3$C$_2$ MXene/NF catalyst required a lower voltage (1.559 V) to receive *j* of 10 mA cm^{-2}.

3.3.2. Commercial zero-gap single cell alkaline anion-exchange membrane water electrolyzer performance

To ensure the high electrocatalytic performance of the synthesized catalysts in zero-gap single AEMWE cell, the electrocatalyst was directly applied as the AEMWE cell electrode, and its activity and durability were monitored (Fig. 7a and S12). Specifically, to test the AEMWE performance, a membrane electrode assembly (MEA) consisting of
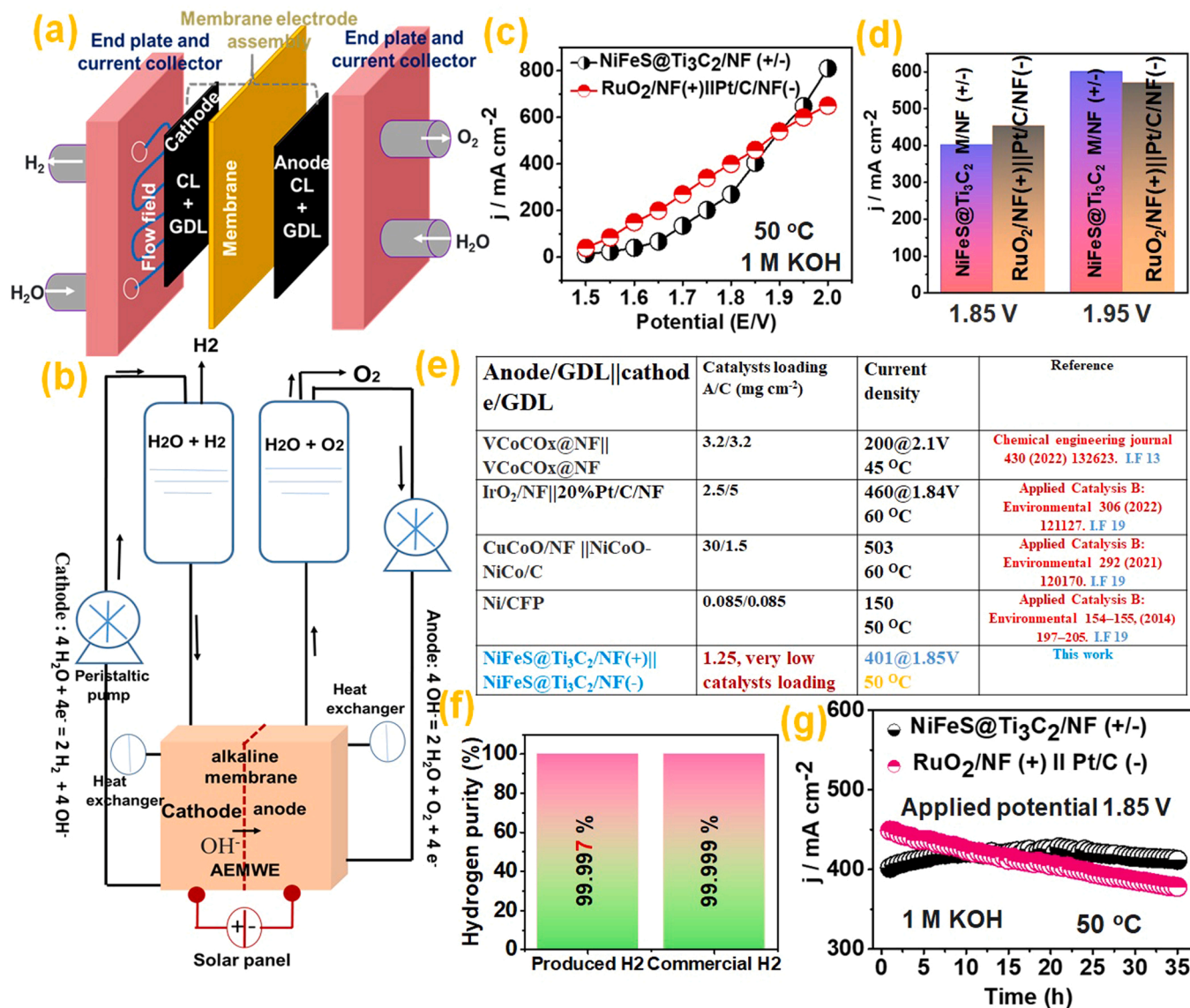
2\T

Fig. 7. (a) Schematic diagram of the AEMWE. (b) Flow chart of AEMWE operation. (c, d) Current–voltage (*I-V*) curve of NiFeS@Ti$_3$C$_2$ MXene/NF. (e) Comparison Table of recent results. (f) Purity of obtained hydrogen. (g) Long-term stability of NiFeS@Ti$_3$C$_2$ MXene/NF. Experimental conditions: 1 M KOH, 50 °C, catalyst loading approximately 1.25 mg cm^{-2}, Pt/C loading approximately 0.3 mg cm^{-2}, and RuO$_2$ loading approximately 0.3 mg cm^{-2}.

NiFeS@Ti$_3$C$_2$ MXene as the cathode as well as anode catalysts with NF as the gas diffusion layer (GDL) and Sustainion X37–50 RT as an anion-exchange membrane was used. A detailed flowchart of electrolyzer operation is shown in Fig. 7b. In this study, at a standard operating cell voltage of 1.85 V, which is the standard operating voltage of industrial alkaline water electrolyzer system, the obtained *j* was 401 mA cm^{-2} with 67.65 % cell efficiency (Section S10 in SI, details in Video 3) for NiFeS@Ti$_3$C$_2$ MXene/NF containing the MEA and 452 mA cm^{-2} for the RuO$_2$/NF= |Pt/C/NF system (Fig. 7c-d). Our electrolyzers show similar performance to other advanced AEMWE systems announced recently (Fig. 7e and Table S2). From a commercial standpoint, our electrolyzers are the best because of low catalyst loading and low operating temperatures, resulting low capital and operating cost. In addition, GC analysis showed that 2.8 mL/min of hydrogen with 99.997 % purity was produced, which meets commercial requirements (Fig. 7f and S13). Furthermore, the durability of the catalyst in the electrolyzer system and the reproducibility of the experimental measurements were assessed: the NiFeS@Ti$_3$C$_2$ MXene/NF electrode showed very high durability for

35 h at potential of 1.85 V. As shown in Fig. 7g, the cell current of the NiFeS@Ti$_3$C$_2$MXene/NF-containing AEMWE increased rapidly up to 16 h because of the activation of the catalyst layer, after which the *j* plateaued and showed a negligible current loss of 0.4 mA/h. Therefore, the device is expected to allow continuous operation for 750 h with a decrease to a minimum j of 100 mA cm^{-2}. Crucially, the NiFeS@-Ti$_3$C$_2$MXene/NF electrode showed a higher durability than the Pt/C/NF= |RuO$_2$/NF electrode pair. Therefore, overall, the results demonstrate the excellent performance of the NiFeS@Ti$_3$C$_2$MXene/NF electrode, and commercial applications are expected.

Supplementary material related to this article can be found online at doi:10.1016/j.apcatb.2022.122039.

The good AEMWE performance of the NiFeS@Ti$_3$C$_2$ MXene/NF GDL can be described by the following reasons:

(1) In an AEMWE, electrochemical reactions occur in a reaction zone having a three-phase boundary (electrolyte, solid electrode, and gaseous product), which provides a sufficient active area for

charge and mass transfer processes. In our experiments, KOH (1 M) was used as the medium, and the electrode surface was wetted to activate the electrode for electrochemical reactions. The maximum intensity of the reaction occurs at the catalyst surface in close contact with the solid membrane electrolyte, where the three-phase boundary is created. In our system, this region was expanded, resulting in a larger catalytically active zone.

(2) NF-coated catalysts as gas diffusion electrodes (GDLs) are commonly used as connectors for catalyst layers, membranes, porous transport layers, and flow fields to promote electron, mass, and heat transfer.

(3) The GDL provides a path for evaluating the liquid electrolytes and gaseous products. In the electrolysis process, a path can distribute the electrolyte at the microscopic level in laminar and turbulent paths and facilitate the electrolyte mass transport pathway to the catalyst surface and to remove gaseous products O_2 and H_2 from the catalyst coating layer as well as preventing the blockage of active sites.

4. Conclusion

In summary, we prepared a $NiFeS@Ti_3C_2$ MXene catalyst on a 3D nickel foam layer by electrochemical and hydrothermal methods, and the resulting catalyst showed superior HER and OER performance, requiring of 180 and 290 mV overpotentials at j of 20 mA cm^{-2}, respectively. Key to our strategy, the electronic coupling and morphology-controlled surface modification of $NiFeS@Ti_3C_2$ MXene/NF electrodes optimized the binding strength between the catalyst surface and *H, *O, and *OOH, thus enhancing the HER and OER process. Furthermore, the self-standing and binder-free 3D $NiFeS@Ti_3C_2$ MXene/NF electrodes exhibited excellent anodic and cathodic activities for water decomposition in a conventional two-electrode electrolyzer and a zero-gap AEMWE. In the two-electrode electrolyzer with $NiFeS@Ti_3C_2$ MXene/NF electrode, the obtained j was 10 mA cm^{-2} at 1.559 V, and a solar panel could drive this voltage. The open porous and binder-free NF gas diffusion layer provided the plenty of active sites for promoted mass and charge transfer, and aided the circulation of the electrolytes and product outgassing. Furthermore, the superior bifunctional $NiFeS@-Ti_3C_2$ MXene/NF electrode showed j of 401 mA cm^{-2} at potential of 1.85 V with 67.65 % cell efficiency in the AEMWE and better stability compared to the Pt/C||RuO_2 cell. Our results show that the membrane electrode assembly containing $NiFeS@Ti_3C_2$ MXene/NF electrodes could replace commercial electrolyzer systems. From a commercial point of view, our electrolyzer are among the best performing AEMWE systems over the recently announced AEMWE systems, because of catalyst loading and low operating temperatures, resulting in low capital and operating costs. We are confident that this result opens a new window for AEMWE commercialization coupled with low-cost green hydrogen production in the future.

CRediT authorship contribution statement

Debabrata Chanda: Conceptualization, Resources, Methodology, Visualization, Formal Investigation, Data curation, Writing – original draft. **Karthik Kannan**: Resources, Validation, Methodology. **Jagadis Gautam**: Resources, Validation, Methodology. **Mikiyas Mekete Meshesha**: Resources, Validation, Methodology. **Seok Gwon Jang**: Resources, Validation, Methodology. **Van An Dinh**: Conceptualization, DFT calculation. **Bee Lyong Yang**: Conceptualization, Project administration, Supervision, Funding acquisition.

Declaration of Competing Interest

The authors declare that they have no financial interests or personal relationships that could affect the work reported in this study.

Data Availability

Data will be made available on request.

Acknowledgments

Appendix A. Supporting information

Supplementary data associated with this article can be found in the online version at doi:10.1016/j.apcatb.2022.122039.

References

[1] Y. Jiao, Y. Zheng, M. Jaroniec, S.Z. Qiao, Design of electrocatalysts for oxygen- and hydrogen-involving energy conversion reactions, Chem. Soc. Rev. 44 (2015) 2060–2086.

[2] J.N. Tiwari, S. Sultan, C.W. Myung, T. Yoon, N. Li, M. Ha, A.M. Harzandi, H. J. Park, D.Y. Kim, S.S. Chandrasekaran, W.G. Lee, V. Vij, H. Kang, T.J. Shin, H. S. Shin, G. Lee, Z. Lee, K.S. Kim, Multicomponent electrocatalyst with ultralow Pt loading and high hydrogen evolution activity, Nat. Energy 3 (2018) 773–782.

[3] T. Alerte, J.P. Edwards, C.M. Gabardo, C.P. O'Brien, A. Gaona, J. Wicks, A. Obradović, A. Sarkar, S.A. Jaffer, H.L. MacLean, D. Sinton, E.H. Sargent, Downstream of the CO₂ electrolyzer: assessing the energy intensity of product separation, ACS Energy Lett. 6 (2021) 4405–4412.

[4] D. Chanda, J. Hnát, M. Paidar, J. Schauer, K. Bouzek, Synthesis and characterization of NiFe2O4 electrocatalyst for the hydrogen evolution reaction in alkaline water electrolysis using different polymer binders, J. Power Sources 285 (2015) 217–226.

[5] K. Zeng, D. Zhang, Recent progress in alkaline water electrolysis for hydrogen production and applications, Prog. Energy Combust. Sci. 36 (2010) 307–326.

[6] F.-C. Shen, S.-N. Sun, Z.-F. Xin, S.-L. Li, L.-Z. Dong, Q. Huang, Y.-R. Wang, J. Liu, Y.-Q. Lan, Hierarchically phosphorus doped bimetallic nitrides arrays with unique interfaces for efficient water splitting, Appl. Catal. B: Environ. 243 (2019) 470–480.

[7] H. Fan, W. Chen, G. Chen, J. Huang, C. Song, Y. Du, C. Li, K. Ostrikov, Plasma-heteroatom-doped Ni-V-Fe trimetallic phospho-nitride as high-performance bifunctional electrocatalyst, Appl. Catal. B: Environ. 268 (2020), 118440.

[8] D. Chanda, J. Hnát, M. Paidar, K. Bouzek, Evolution of physicochemical and electrocatalytic properties of NiCo2O4 (AB2O4) spinel oxide with the effect of Fe substitution at the A site leading to efficient anodic O2 evolution in an alkaline environment, Int. J. Hydrogen Energy 39 (2014) 5713–5722.

[9] D. Chanda, J. Hnát, T. Bystron, M. Paidar, K. Bouzek, Optimization of synthesis of the nickel-cobalt oxide based anode electrocatalyst and of the related membrane-electrode assembly for alkaline water electrolysis, J. Power Sources 347 (2017) 247–258.

[10] A. Li, L. Zhang, F. Wang, L. Zhang, L. Li, H. Chen, Z. Wei, Rational design of porous Ni-Co-Fe ternary metal phosphides nanobricks as bifunctional electrocatalysts for efficient overall water splitting, Appl. Catal. B: Environ. 310 (2022), 121353.

[11] S. Yang, J.-Y. Zhu, X.-N. Chen, M.-J. Huang, S.-H. Cai, J.-Y. Han, J.-S. Li, Self-supported bimetallic phosphides with artificial heterointerfaces for enhanced electrochemical water splitting, Appl. Catal. B: Environ. 304 (2022), 120914.

[12] S. Liu, Y. Xu, D. Chanda, L. Tan, R. Xing, X. Li, L. Mao, N. Kazuya, A. Fujishima, Ultrathin WS2 nanosheets vertically aligned on TiO2 nanobelts as efficient alkaline hydrogen evolution electrocatalyst, Int. J. Hydrogen Energy 45 (2020) 1697–1705.

[13] C. Wang, M. Zhu, Z. Cao, P. Zhu, Y. Cao, X. Xu, C. Xu, Z. Yin, Heterogeneous bimetallic sulfides based seawater electrolysis towards stable industrial-level large current density, Appl. Catal. B: Environ. 291 (2021), 120071.

[14] D. Chanda, R.A. Tufa, Y.Y. Birdja, S. Basu, S. Liu, Hydrothermally/electrochemically decorated FeSe on Ni-foam electrode: an efficient bifunctional electrocatalysts for overall water splitting in an alkaline medium, Int. J. Hydrogen Energy 45 (2020) 27182–27192.

[15] J. Huang, S. Wen, G. Chen, W. Chen, G. Wang, H. Fan, D. Chen, C. Song, M. Li, X. Wang, L. Li, M. Tao, B. Li, X. Wang, K. Ostrikov, Multiphase Ni-Fe-selenide nanosheets for highly-efficient and ultra-stable water electrolysis, Appl. Catal. B: Environ. 277 (2020), 119220.

[16] X. Luan, X. Du, Y. Kong, F. Qu, L. Lu, A novel FeS–NiS hybrid nanoarray: an efficient and durable electrocatalyst for alkaline water oxidation, Chem. Commun. 55 (2019) 7335–7338.

[17] J. Xie, J. Zhang, S. Li, F. Grote, X. Zhang, H. Zhang, R. Wang, Y. Lei, B. Pan, Y. Xie, Controllable disorder engineering in oxygen-incorporated MoS2 ultrathin nanosheets for efficient hydrogen evolution, J. Am. Chem. Soc. 135 (2013) 17881–17888.

[18] J. Xie, H. Zhang, S. Li, R. Wang, X. Sun, M. Zhou, J. Zhou, X.W. Lou, Y. Xie, Defect-rich MoS2 ultrathin nanosheets with additional active edge sites for enhanced electrocatalytic hydrogen evolution, Adv. Mater. 25 (2013) 5807–5813.

[19] Y. Zeng, Y. Meng, Z. Lai, X. Zhang, M. Yu, P. Fang, M. Wu, Y. Tong, X. Lu, An ultrastable and high-performance flexible fiber-shaped Ni–Zn battery based on a Ni–NiO heterostructured nanosheet cathode, Adv. Mater. 29 (2017) 1702698.

[20] J. Xie, H. Qu, J. Xin, X. Zhang, G. Cui, X. Zhang, J. Bao, B. Tang, Y. Xie, Defect-rich MoS2 nanowall catalyst for efficient hydrogen evolution reaction, Nano Res. 10 (2017) 1178–1188.

[21] J. Xie, J. Xin, G. Cui, X. Zhang, L. Zhou, Y. Wang, W. Liu, C. Wang, M. Ning, X. Xia, Y. Zhao, B. Tang, Vertically aligned oxygen-doped molybdenum disulfide nanosheets grown on carbon cloth realizing robust hydrogen evolution reaction, Inorg. Chem. Front. 3 (2016) 1160–1166.

[22] J. Xie, S. Li, X. Zhang, J. Zhang, R. Wang, H. Zhang, B. Pan, Y. Xie, Atomically-thin molybdenum nitride nanosheets with exposed active surface sites for efficient hydrogen evolution, Chem. Sci. 5 (2014) 4615–4620.

[23] D. Jia, L. Han, Y. Li, W. He, C. Liu, J. Zhang, C. Chen, H. Liu, H.L. Xin, Optimizing electron density of nickel sulfide electrocatalysts through sulfur vacancy engineering for alkaline hydrogen evolution, J. Mater. Chem. A 8 (2020) 18207–18214.

[24] W. Chen, E.J.G. Santos, W. Zhu, E. Kaxiras, Z. Zhang, Tuning the electronic and chemical properties of monolayer MoS2 adsorbed on transition metal substrates, Nano Lett. 13 (2013) 509–514.

[25] X. Meng, L. Yu, C. Ma, B. Nan, R. Si, Y. Tu, J. Deng, D. Deng, X. Bao, Three-dimensionally hierarchical MoS2/graphene architecture for high-performance hydrogen evolution reaction, Nano Energy 61 (2019) 611–616.

[26] K. Guruprasad, T. Maiyalagan, S. Shanmugam, Phosphorus doped MoS2 nanosheet promoted with nitrogen, sulfur dual doped reduced graphene oxide as an effective electrocatalyst for hydrogen evolution reaction, ACS Appl. Energy Mater. 2 (2019) 6184–6194.

[27] H. Huang, W. Huang, Z. Yang, J. Huang, J. Lin, W. Liu, Y. Liu, Strongly coupled MoS2 nanoflake–carbon nanotube nanocomposite as an excellent electrocatalyst for hydrogen evolution reaction, J. Mater. Chem. A 5 (2017) 1558–1566.

[28] T. Dong, X. Zhang, P. Wang, H.-S. Chen, P. Yang, Formation of Ni-doped MoS2 nanosheets on N-doped carbon nanotubes towards superior hydrogen evolution, Electrochim. Acta 338 (2020), 135885.

[29] H. Li, Y. Wen, X. Zhu, J. Wang, L. Zhang, B. Sun, Novel heterostructure of a MXene@NiFe-LDH nanohybrid with superior peroxidase-like activity for sensitive colorimetric detection of glutathione, ACS Sustain. Chem. Eng. 8 (2020) 520–526.

[30] O. Mashtalir, M.R. Lukatskaya, M.-Q. Zhao, M.W. Barsoum, Y. Gogotsi, Amine-assisted delamination of Nb2C MXene for Li-ion energy storage devices, Adv. Mater. 27 (2015) 3501–3506.

[31] M. Naguib, V.N. Mochalin, M.W. Barsoum, Y. Gogotsi, 25th anniversary article: MXenes: a new family of two-dimensional materials, Adv. Mater. 26 (2014) 992–1005.

[32] R. Lukatskaya Maria, O. Mashtalir, E. Ren Chang, Y. Dall'Agnese, P. Rozier, L. Taberna Pierre, M. Naguib, P. Simon, W. Barsoum Michel, Y. Gogotsi, Cation intercalation and high volumetric capacitance of two-dimensional titanium carbide, Science 341 (2013) 1502–1505.

[33] P.V. Shinde, P. Mane, B. Chakraborty, C. Sekhar Rout, Spinel NiFe2O4 nanoparticles decorated 2D Ti3C2 MXene sheets for efficient water splitting: experiments and theories, J. Colloid Interface Sci. 602 (2021) 232–241.

[34] M. Han, J. Yang, J. Jiang, R. Jing, S. Ren, C. Yan, Efficient tuning the electronic structure of N-doped Ti-based MXene to enhance hydrogen evolution reaction, J. Colloid Interface Sci. 582 (2021) 1099–1106.

[35] H. Lin, S. Gao, C. Dai, Y. Chen, J. Shi, A two-dimensional biodegradable niobium carbide (MXene) for photothermal tumor eradication in NIR-I and NIR-II biowindows, J. Am. Chem. Soc. 139 (2017) 16235–16247.

[36] X. Li, X. Lv, X. Sun, C. Yang, Y.-Z. Zheng, L. Yang, S. Li, X. Tao, Edge-oriented, high-percentage 1T′-phase MoS2 nanosheets stabilize Ti3C2 MXene for efficient electrocatalytic hydrogen evolution, Appl. Catal. B: Environ. 284 (2021), 119708.

[37] G. Kresse, J. Furthmüller, Efficiency of ab-initio total energy calculations for metals and semiconductors using a plane-wave basis set, Comput. Mater. Sci. 6 (1996) 15–50.

[38] G. Kresse, J. Furthmüller, Efficient iterative schemes for ab initio total-energy calculations using a plane-wave basis set, Phys. Rev. B 54 (1996) 11169.

[39] J.P. Perdew, K. Burke, M. Ernzerhof, Generalized gradient approximation made simple, Phys. Rev. Lett. 77 (1996) 3865.

[40] G. Kresse, D. Joubert, From ultrasoft pseudopotentials to the projector augmented-wave method, Phys. Rev. B 59 (1999) 1758.

[41] S. Grimme, J. Antony, S. Ehrlich, H. Krieg, A consistent and accurate ab initio parametrization of density functional dispersion correction (DFT-D) for the 94 elements H-Pu, J. Chem. Phys. 132 (2010), 154104.

[42] S. Kumar, M.A. Rehman, S. Lee, M. Kim, H. Hong, J.-Y. Park, Y. Seo, Supercapacitors based on Ti3C2Tx MXene extracted from supernatant and current collectors passivated by CVD-graphene, Sci. Rep. 11 (2021) 649.

[43] Q. Wu, Y. Wang, P. Li, S. Chen, F. Wu, MXene titanium carbide synthesized by hexagonal titanium aluminum carbide with high specific capacitance and low impedance, Dalton Trans. 51 (2022) 3263–3274.

[44] C. Simon, J. Zander, T. Kottakkat, M. Weiss, J. Timm, C. Roth, R. Marschall, Fast microwave synthesis of phase-pure Ni2FeS4 thiospinel nanosheets for application in electrochemical CO2 reduction, ACS Appl. Energy Mater. 4 (2021) 8702–8708.

[45] G. Zhao, H. Lv, Y. Zhou, X. Zheng, C. Wu, C. Xu, Self-assembled sandwich-like mxene-derived nanocomposites for enhanced electromagnetic wave absorption, ACS Appl. Mater. Interfaces 10 (2018) 42925–42932.

[46] P. Ganesan, A. Sivanantham, S. Shanmugam, Inexpensive electrochemical synthesis of nickel iron sulphides on nickel foam: super active and ultra-durable electrocatalysts for alkaline electrolyte membrane water electrolysis, J. Mater. Chem. A 4 (2016) 16394–16402.

[47] X. Ding, Y. Li, C. Li, W. Wang, L. Wang, L. Feng, D. Han, 2D visible-light-driven TiO2@Ti3C2/g-C3N4 ternary heterostructure for high photocatalytic activity, J. Mater. Sci. 54 (2019) 9385–9396.

[48] Y. Gong, R. Tu, T. Goto, High-speed deposition of titanium carbide coatings by laser-assisted metal–organic CVD, Mater. Res. Bull. 48 (2013) 2766–2770.

[49] T. Schultz, N.C. Frey, K. Hantanasirisakul, S. Park, S.J. May, V.B. Shenoy, Y. Gogotsi, N. Koch, Surface termination dependent work function and electronic properties of Ti3C2Tx MXene, Chem. Mater. 31 (2019) 6590–6597.

[50] X. Wang, Y. Xie, B. Bateer, K. Pan, Y. Zhou, Y. Zhang, G. Wang, W. Zhou, H. Fu, Hexagonal FeS nanosheets with high-energy (001) facets: counter electrode materials superior to platinum for dye-sensitized solar cells, Nano Res. 9 (2016) 2862–2874.

[51] Z. Jing, Q. Zhao, D. Zheng, L. Sun, J. Geng, Q. Zhou, J. Lin, Nickel-doped pyrrhotite iron sulfide nanosheets as a highly efficient electrocatalyst for water splitting, J. Mater. Chem. A 8 (2020) 20323–20330.

[52] X. Wang, Y. Zhang, H. Si, Q. Zhang, J. Wu, L. Gao, X. Wei, Y. Sun, Q. Liao, Z. Zhang, K. Ammarah, L. Gu, Z. Kang, Y. Zhang, Single-atom vacancy defect to trigger high-efficiency hydrogen evolution of MoS2, J. Am. Chem. Soc. 142 (2020) 4298–4308.

[53] X. Wang, J. Bai, Y. Wang, X. Lu, Z. Zou, J. Huang, C. Xu, Sulfur vacancies-doped Sb2S3 nanorods as high-efficient electrocatalysts for dinitrogen fixation under ambient conditions, Green Energy Environ. 7 (2022) 755–762.

[54] Z. He, Y. Wang, X. Dong, N. Zheng, H. Ma, X. Zhang, Indium sulfide nanotubes with sulfur vacancies as an efficient photocatalyst for nitrogen fixation, RSC Adv. 9 (2019) 21646–21652.

[55] Y. Lin, K. Sun, S. Liu, X. Chen, Y. Cheng, W.-C. Cheong, Z. Chen, L. Zheng, J. Zhang, X. Li, Y. Pan, C. Chen, Construction of CoP/NiCoP nanotadpoles heterojunction interface for wide pH hydrogen evolution electrocatalysis and supercapacitor, Adv. Energy Mater. 9 (2019) 1901213.

[56] L. Li, D. Yu, P. Li, H. Huang, D. Xie, C.-C. Lin, F. Hu, H.-Y. Chen, S. Peng, Interfacial electronic coupling of ultrathin transition-metal hydroxide nanosheets with layered MXenes as a new prototype for platinum-like hydrogen evolution, Energy Environ. Sci. 14 (2021) 6419–6427.

[57] S. Anantharaj, H. Sugime, B. Chen, N. Akagi, S. Noda, Achieving increased electrochemical accessibility and lowered oxygen evolution reaction activation energy for Co2+ sites with a simple anion preoxidation, J. Phys. Chem. C 124 (2020) 9673–9684.

[58] Y. Zhang, J. Xu, L. Lv, A. Wang, B. Zhang, Y. Ding, C. Wang, Electronic engineering of CoSe/FeSe2 hollow nanospheres for efficient water oxidation, Nanoscale 12 (2020) 10196–10204.

[59] L. Xiu, Z. Wang, M. Yu, X. Wu, J. Qiu, Aggregation-resistant 3D MXene-based architecture as efficient bifunctional electrocatalyst for overall water splitting, ACS Nano 12 (2018) 8017–8028.

[60] C.-F. Du, K.N. Dinh, Q. Liang, Y. Zheng, Y. Luo, J. Zhang, Q. Yan, Self-assemble and in situ formation of Ni1−xFexPS3 nanomosaic-decorated MXene hybrids for overall water splitting, Adv. Energy Mater. 8 (2018) 1801127.

[61] M. Islam, D.T. Tran, T.H. Nguyen, V.A. Dinh, N.H. Kim, J.H. Lee, Efficient synergism of NiO-NiSe2 nanosheet-based heterostructures shelled titanium nitride array for robust overall water splitting, J. Colloid Interface Sci. 612 (2022) 121–131.

[62] P. Xu, H. Wang, J. Liu, X. Feng, W. Ji, C.-T. Au, High-performance NixCo3-xO4/ Ti3C2Tx-HT interfacial nanohybrid for electrochemical overall water splitting, ACS Appl. Mater. Interfaces 13 (2021) 34308–34319.

[63] Q. Yue, J. Sun, S. Chen, Y. Zhou, H. Li, Y. Chen, R. Zhang, G. Wei, Y. Kang, Hierarchical mesoporous MXene–NiCoP electrocatalyst for water-splitting, ACS Appl. Mater. Interfaces 12 (2020) 18570–18577.

[64] D. Guo, X. Li, Y. Jiao, H. Yan, A. Wu, G. Yang, Y. Wang, C. Tian, H. Fu, A dual-active Co-CoO heterojunction coupled with Ti3C2-MXene for highly-performance overall water splitting, Nano Res. 15 (2022) 238–247.

[65] Y. Li, T. Dai, Q. Wu, X. Lang, L. Zhao, Q. Jiang, Design heterostructure of NiS–NiS2 on NiFe layered double hydroxide with Mo doping for efficient overall water splitting, Mater. Today Energy 23 (2022), 100906.

[66] F.-S. Zhang, J.-W. Wang, J. Luo, R.-R. Liu, Z.-M. Zhang, C.-T. He, T.-B. Lu, Extraction of nickel from NiFe-LDH into Ni2P@NiFe hydroxide as a bifunctional electrocatalyst for efficient overall water splitting, Chem. Sci. 9 (2018) 1375–1384.

[67] L.-M. Cao, Y.-W. Hu, S.-F. Tang, A. Iljin, J.-W. Wang, Z.-M. Zhang, T.-B. Lu, Fe-CoP electrocatalyst derived from a bimetallic prussian blue analogue for large-current-density oxygen evolution and overall water splitting, Adv. Sci. 5 (2018) 1800949.

[68] C. Kim, S.H. Kim, S. Lee, I. Kwon, S.H. Kim, S. Kim, C. Seok, Y.S. Park, Y. Kim, Boosting overall water splitting by incorporating sulfur into NiFe (oxy)hydroxide, J. Energy Chem. 64 (2022) 364–371.

[69] V. Ramalingam, P. Varadhan, H.-C. Fu, H. Kim, D. Zhang, S. Chen, L. Song, D. Ma, Y. Wang, H.N. Alshareef, J.-H. He, Heteroatom-mediated interactions between ruthenium single atoms and an MXene support for efficient hydrogen evolution, Adv. Mater. 31 (2019) 1903841.

[70] J.K. Nørskov, T. Bligaard, A. Logadottir, J. Kitchin, J.G. Chen, S. Pandelov, U. Stimming, Trends in the exchange for hydrogen evolution, J. Electrochem. Soc. 152 (2005) J23.

[71] K. Chang, D.T. Tran, J. Wang, S. Prabhakaran, D.H. Kim, N.H. Kim, J.H. Lee, Atomic heterointerface engineering of Ni2P-NiSe2 nanosheets coupled znp-based arrays for high-efficiency solar-assisted water splitting, Adv. Funct. Mater. (2022) 2113224.

[72] Y. Chen, H. Yao, F. Kong, H. Tian, G. Meng, S. Wang, X. Mao, X. Cui, X. Hou, J. Shi, V2C MXene synergistically coupling FeNi LDH nanosheets for boosting oxygen evolution reaction, Appl. Catal. B 297 (2021), 120474.

[73] J. Zhu, L. Hu, P. Zhao, L.Y.S. Lee, K.-Y. Wong, Recent advances in electrocatalytic hydrogen evolution using nanoparticles, Chem. Rev. 120 (2020) 851–918.

[74] T. Bligaard, J.K. Nørskov, Ligand effects in heterogeneous catalysis and electrochemistry, Electrochim. Acta 52 (2007) 5512–5516.

[75] P. Xiong, X. Zhang, H. Wan, S. Wang, Y. Zhao, J. Zhang, D. Zhou, W. Gao, R. Ma, T. Sasaki, G. Wang, Interface modulation of two-dimensional superlattices for efficient overall water splitting, Nano Lett. 19 (2019) 4518–4526.

[76] W. Li, X. Gao, D. Xiong, F. Wei, W.-G. Song, J. Xu, L. Liu, Hydrothermal synthesis of monolithic Co3Se4 nanowire electrodes for oxygen evolution and overall water splitting with high efficiency and extraordinary catalytic stability, Adv. Energy Mater. 7 (2017) 1602579.

[77] Z. Kang, H. Guo, J. Wu, X. Sun, Z. Zhang, Q. Liao, S. Zhang, H. Si, P. Wu, L. Wang, Y. Zhang, Engineering an earth-abundant element-based bifunctional electrocatalyst for highly efficient and durable overall water splitting, Adv. Funct. Mater. 29 (2019) 1807031.

[78] J. Liu, J. Wang, B. Zhang, Y. Ruan, L. Lv, X. Ji, K. Xu, L. Miao, J. Jiang, Hierarchical NiCo2S4@NiFe LDH heterostructures supported on nickel foam for enhanced overall-water-splitting activity, ACS Appl. Mater. Interfaces 9 (2017) 15364–15372.

[79] Y. Liu, S. Jiang, S. Li, L. Zhou, Z. Li, J. Li, M. Shao, Interface engineering of (Ni, Fe) S2@MoS2 heterostructures for synergetic electrochemical water splitting, Appl. Catal. B: Environ. 247 (2019) 107–114.

[80] Y. Xie, H. Yu, L. Deng, R.S. Amin, D. Yu, A.E. Fetohi, M.Y. Maximov, L. Li, K.M. El-Khatib, S. Peng, Anchoring stable FeS2 nanoparticles on MXene nanosheets via interface engineering for efficient water splitting, Inorg. Chem. Front. 9 (2022) 662–669.

[81] J. Yu, G. Cheng, W. Luo, Ternary nickel–iron sulfide microflowers as a robust electrocatalyst for bifunctional water splitting, J. Mater. Chem. A 5 (2017) 15838–15844.